RESEARCH PAPER

Structural and Optoelectronic Characterization of Graphene-ZnO/Si Nano Hybrid Photodetector

Zahra M. Talib, Azhar I. Hassan *, *Jehan A. Saimon*

Laser Science and Technology branch, Department of Applied Sciences, University of Technology, Iraq

ABSTRACT

Graphene-ZnO nanohybrid thin films were prepared by the spray pyrolysis technique at 350 °C with graphene nanoplate concentrations of 0.1, 0.2, 0.3, 0.4, and 0.5 wt.% deposited on quartz and silicon substrates. The structural and electrical properties have been investigated. XRD results show that the films have a hexagonal wurtzite polycrystalline structure. AFM images showed how the grains are distributed and arranged on the surfaces and illustrated the effect of graphene concentration on the properties of the film by measuring the roughness and grain size. FESEM showed that the surface of the film without graphene is covered with high-packing hexagonal grains with a narrow grain size distribution. At a higher graphene content of 0.5 wt.%, graphene nanoplates distributed within the ZnO matrix were observed. The current-voltage characteristics of the heterojunction show a typical rectification behavior. The photocurrent under illumination measurement has increased gradually with increasing light intensity and graphene concentration. The capacitance-voltage characteristics show that the built-in potential barrier (Vbi) value ranges from 0.65 V for ZnO/Si to 0.3 V for G-ZnO/Si with 0.5 graphene. The spectral responsivity of the photodetector was enhanced for the G-ZnO hybrid at 0.5 graphene.

INTRODUCTION

The use of carbon nanomaterials in optoelectronic devices has been the subject of intense research in the last decades, showing great potential for significantly improving device properties like efficiency and durability [1]. The change of these properties results from the method and conditions of preparation and the percentage of impurities found in the material. Graphene consists of a single sheet of hexagonally arranged carbon atoms with sp2 hybridization, providing a high specific surface area [1].

It has been paid massive attention in the past decade because of its fascinating characteristics, including high conductivity, good transparency, high carrier mobility, and electromechanical modulation. By these tokens, graphene has become one of the most popular materials for application in various optoelectronic devices, e.g., solar cells, light-emitting diodes (LEDs), and photodetectors (PDs). As for PDs applications, researchers have successfully developed various high-performance photodetectors based on graphene and other semiconductor materials e.g., ZnO [2].

Zinc oxide is an II-VI group n-type semiconducting material that holds a critical

* *Corresponding Author Email: azhar.hassan@yahoo.com*

position because of its transparency in the visible range with a wide bandgap (~3.37 eV) and large exciton binding energy (60 meV) [3, 4, 5]. Zinc oxide (ZnO) has become one of the generality popular metal oxides for optoelectronic implementations [6, 7,1]. Moreover, one-dimensional ZnO nanostructures have exclusive electron transport characteristics, making them ideal for integration into devices like field-effect transistors [8]. One of the generality good and cost-effective techniques for controlling the bandgap, morphology, and ZnO nanostructures surface defect states are the fabrication of nanocomposites dependent on ZnO and graphene or graphene Oxide [9]. In terms of graphene, its unique features, such as massless Dirac electrons around the K point, rise carrier mobility, room-temperature quantum Hall effect, and interaction with other nanomaterials, are becoming increasingly popular [10, 11]. Contact with other materials can change graphene's physical and chemical properties, affecting its performance in devices. Graphene hybridizations with ZnO nanoparticles and vertical nanostructures have superior photovoltaic characteristics than graphene or ZnO alone in solar cells [2, 12] and photocatalysts [13-16], despite their varied morphologies.

The sensitivity of ZnO can be improved by combining it with carbon-based nanomaterials (graphene, carbon nanotubes) in combinations and hybrid structures and shrinking its dimensions down to nanostructures. Research of single interfaces of graphene ZnO revealed that graphene could efficiently separate photoinduced excitons shaped in ZnO by acting as an extraordinary electron acceptor and transport material. This property makes graphene and ZnO a promising combination for optoelectronic devices, gas sensors, and biological sensors, where graphene can act as a highly conducting mesh. The junction interface resistance, in turn, has a significant impact on sensor performance. [17]

In this work, the goal is to study the influence of graphene on the ZnO/Si heterojunction by analyzing its photoelectric behavior. Thus, the graphene that was added to the ZnO thin films was deposited on quartz and silicon using the spray pyrolysis technique. To investigate the properties of the hybrid system, the morphology, topography, I-V behavior, built-in potential (Vbi), and responsivity of the photodetector have all been examined.

MATERIALS AND METHODS

Graphene-ZnO thin films were deposited on quartz and silicon substrate by spray pyrolysis. Spray solution with $ZnCl_2$ (HIMEDIA zinc chloride 99.0%) to make Zinc Oxide thin films and then add graphene (Skyspring Nanomaterials, Inc, USA, thickness 6-8 nm, electrical conductivity 10^7 S.m^{-1}) with various concentrations (0, 0.1, 0.2, 0.3, 0.4 and 0.5 wt.%). The graphene nanoplates were dispersed in distilled water using a magnetic stirrer. To eliminate contamination, the quartz and silicon substrates were cleaned by sonication in ethanol. The solution was deposited on a substrate heated at 350 °C and a 4 ml/min solution flow rate. The distance between the nozzle end and the substrate was about 30 cm. XRD diffractometer (XRD 6000, Shimadzu, Japan) with wavelength (1.5406 Å for CuKα) was used to analyze the phases and crystalline structure. Structural properties were studied to determine the root mean square roughness, and grain size distribution of graphene-ZnO thin films by atomic force microscope (AFM) with (NT-MDT, Ntegra, Russia) and Scanning Electron Microscopy (SEM). An Keithley electrometer was used to study the I-V characteristics of the prepared junctions. C-V characteristics of the heterojunction under test were measured using a precision impedance analyzer from (Agilent, 4294A, USA). Spectral responsivity can be determined using a spectral range of a monochromatic light source (300-1000).

RESULTS AND DISCUSSION

XRD patterns of ZnO and graphene-ZnO thin films, all set at 350 °C temperature, were demonstrated in Fig. 1. This figure confirmed the Zinc Oxide phases of the hexagonal wurtzite structure. All the crystalline planes (100), (002), (101), (102), (110), and (103) of the ZnO were evident, and (002) was the favored orientation. Results show that the XRD patterns of graphene-ZnO nanohybrids were almost comparable to that of the pure ZnO films, where no additional phases have been distinguished. On the other hand, the addition of graphene does not modify the crystal orientations or result in variation in ZnO preferred orientations. No diffraction peaks of graphene have been observed in the thin film patterns, as the quantities of graphene were too small to be detected by the XRD technique, and the yield of graphene diffraction intensity is much lower than the yield of the diffraction intensity of zinc oxide

[18, 19, 20, 21].

To investigate the influence of graphene content on the surface morphologies of the ZnO films, FESEM images were studied for all films, as shown in Fig. 2. The images showed several morphological features on the films deposited under various graphene content were obtained. Zinc oxide film surface without graphene is covered with high packing hexagonal grains having a sharp crystal edge and narrow grain size distribution. With the addition of graphene as low as 0.1 wt.%, the zinc oxide crystals develop a more refined grain with few grains that must undergo excessive growth. Also, the packing density of the grain has noticeably decreased. As the percentage of graphene gradually increased, more random orientation of grains has obtained with finer grain size. At a higher graphene content of 0.5 wt.%, graphene nanoplates nested with zinc oxide grains were observed.

Results suggest that the graphene nanoplate strongly acted as grain growth inhibitors, which may explain the X-ray diffraction results of the films. As the size of the ZnO grains decreases, the total area of the grain boundaries increases, and the crystallite sizes decrease, thus increasing the structural defects and hence increasing the dislocation density. This was reflected in the decrease of the degree of crystallization of the films with adding more graphene nanoplates, which causes a reduction in the relative intensity of the diffraction patterns, as has been noticed with the most dominant plane (002).

Atomic force microscopy (AFM) analysis was used to study the surface topography and surface crystal structure of G-ZnO thin films because studying the surfaces of the films is essential in understanding how the grains are distributed and arranged on the surfaces and studying the effect of graphene concentration on the properties of the film by measuring the degree of roughness, RMS and grain size.

Fig. 3 displays the topographical analytical images of the surface roughness in two dimensions
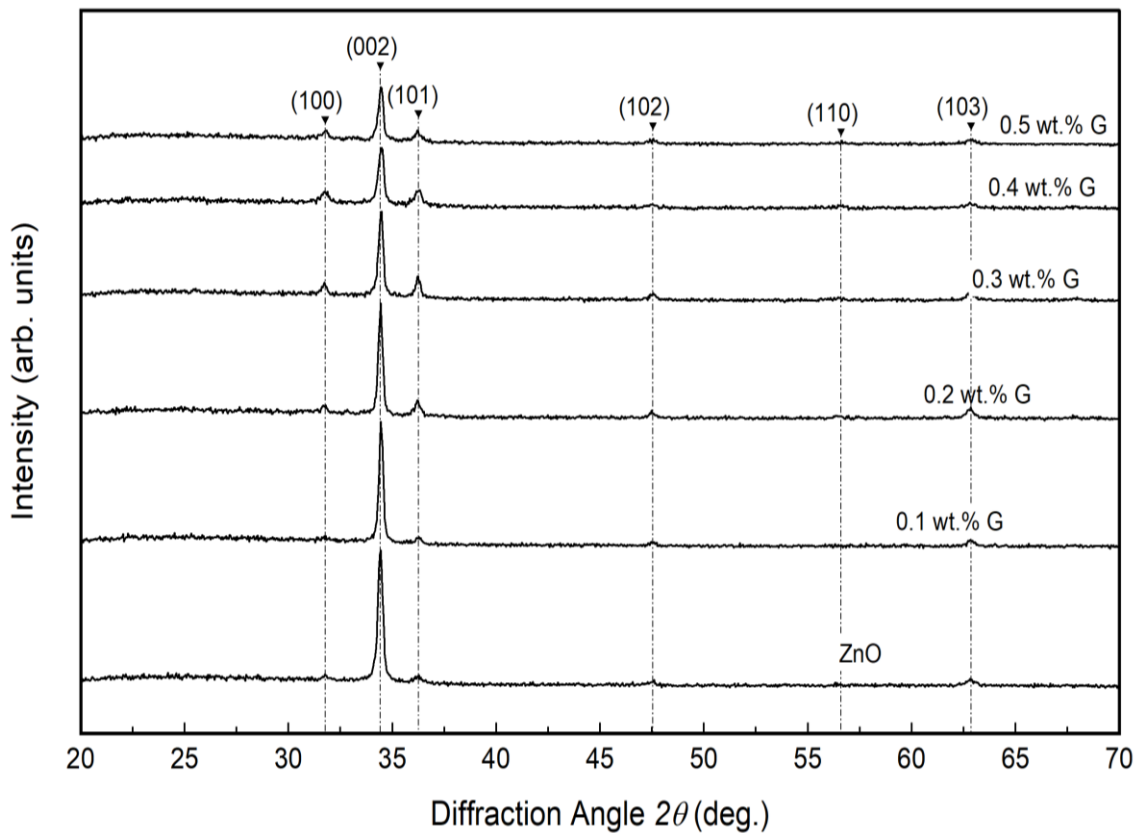

Fig. 1. XRD pattern of ZnO-graphene thin films.

for a measuring area (3 µm × 3 µm) of G-ZnO thin films with various concentrations of graphene (0.1, 0.2, 0.3, 0.4, 0.5). It shows a regular propagation of a granulated ZnO grain structure that is reliable with a superior-quality of nanostructure of ZnO thin film with a pin-hole-free, crack-free, and smooth surface. This image shows that the prepared ZnO thin film surface comprises extremely crystalline grains with hexagonal nanoparticles. The surface of the film consists of several granulated particles with uniform sizes, and the particle per crystallite size is raised as the graphene concentration grows. As the grain size enlarged, the thin film surface designed structures island-shaped, which managed to a rougher surface.

The AFM images of both pure ZnO and G–ZnO films, as revealed in Fig. 3 a–d), display that the deposited films are smooth and uniform. Wt.
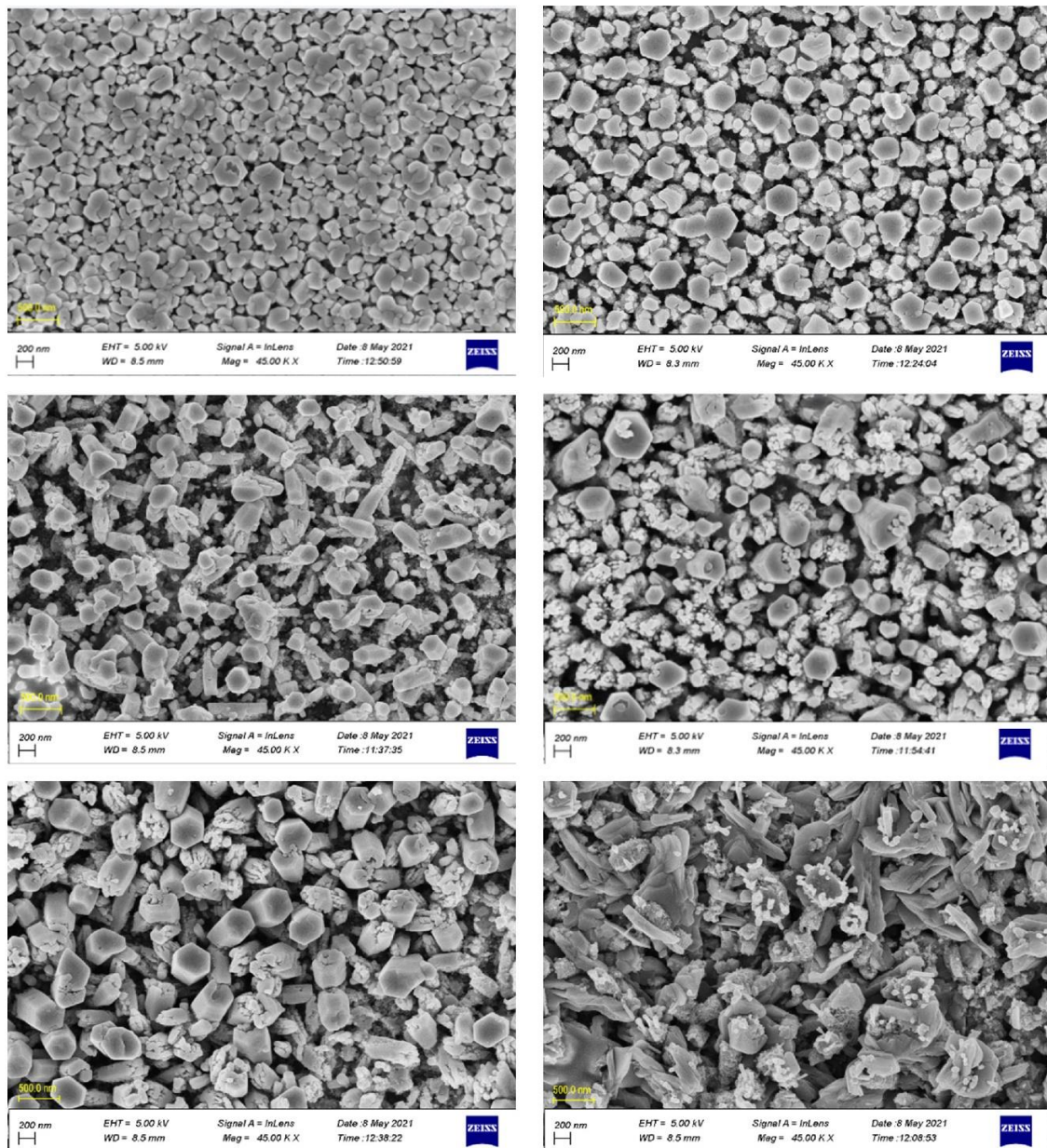

Fig. 2. FESEM images of ZnO-G thin film morphologies with various graphene content.

% G–ZnO films demonstrate irregularly shaped graphene sheets extending a few micrometers in length. The sheet of graphene introduced higher roughness to the surface. The morphology of the surface is formed via tiny grains. As the deposition further rises, the large structure concentration constantly propagates in height, and lateral size inclines to display a mounds-like structure. There is a rise of the large structure that raises in height and width together, inclining to show a stepped pyramid-like structure.

Table 1 shows the relation between grain size, roughness, and root mean square (RMS) for G-ZnO thin films with different concentrations. The graphene sheet yielded higher surface roughness.

The electrical conductivity of the prepared thin films was calculated as a temperature function and is specified in Fig. 4. This figure shows the film conductivity increases as temperature increases, and this proposes that the specimens demonstrate a semiconducting attitude. The conductivity increases as graphene concentration increases due to increased crystalline size and decreased scattering at the grain boundary since the grain boundary region operates as the critical origin for trapping free carriers. The grain size and crystallinity production produce more excellent conductivity.
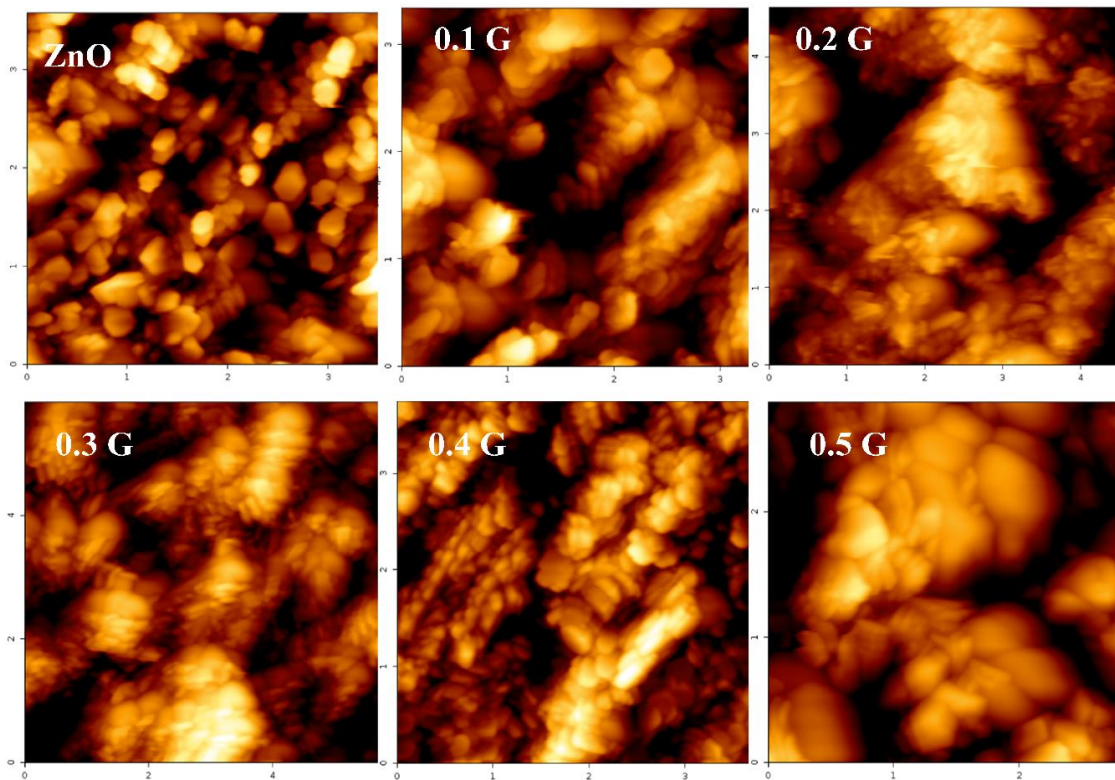

Fig. 3. AFM images of ZnO-G thin film morphologies with various graphene content.

Table 1. Lattice parameters of graphene-ZnO thin films at different concentrations.

Sample	Grain Size (nm)	Roughness (nm)	RMS
ZnO	54.13	36.24	47.88
0.1G	19.08	40.98	53.98
0.2G	17.56	72.16	91.14
0.3G	10.19	85.81	106.0
0.4G	63.21	43.43	53.94
0.5G	35.93	33.69	42.41

The conductivity plots of ZnO, 0.1 G-ZnO, and 0.4 G-ZnO reveal two slopes demonstrating two various conduction mechanisms, whereas (0.2, 0.3, 0.5) G-ZnO thin films show a linear behavior. The conductivity mechanism in ZnO films is controlled through two various thermally
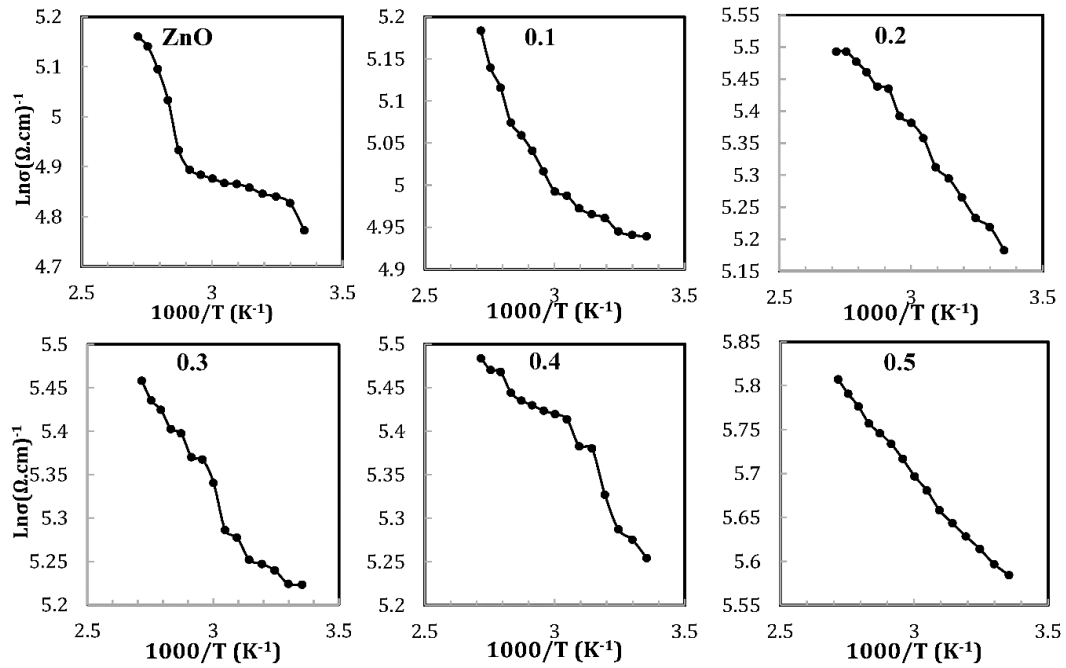

Fig. 4. Conductivity as a function of the temperature of G -ZnO thin films with various graphene content.
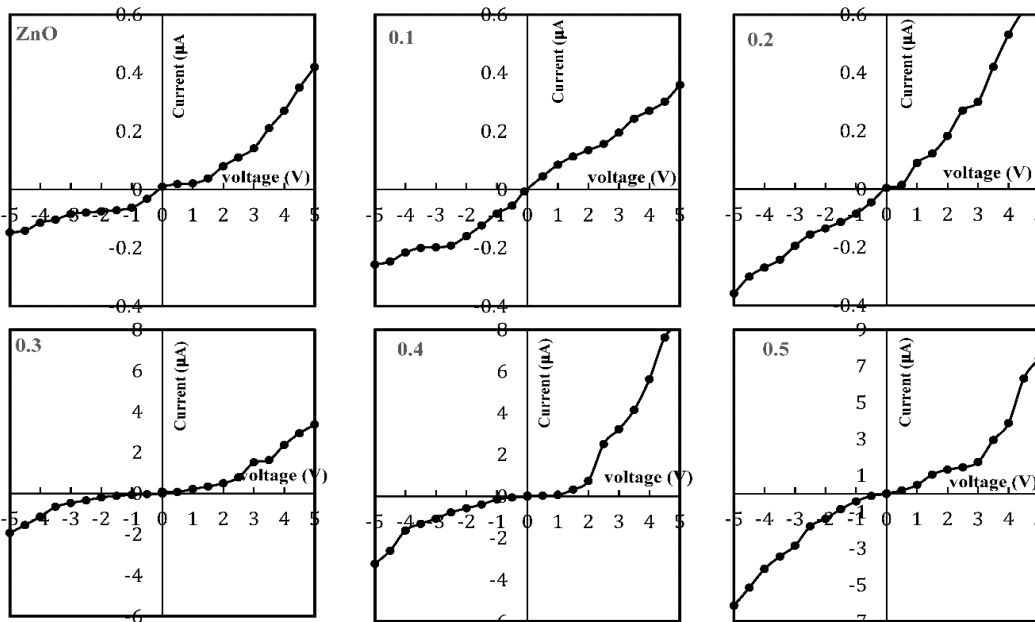

Fig. 5. Dark I-V characteristic of G -ZnO thin films with various graphene content.

activated conduction processes occurring at different energy levels. ΔEI and ΔEII represent the activation energy values for (low-temperature region I) and (high-temperature region II) which match the energy alteration among the donor and conduction levels. Correspondingly, ZnO, 0.1 G-ZnO, and 0.4 G-ZnO samples had ΔEI values of 0.0471, 0.0309, and 0.0303 eV at low

temperatures. The gained ΔEI values outcomes due to deep levels under the conduction band. The amount of ΔEI value decease with graphene concentration. The ΔEII values at all temperatures ZnO, and (0.1, 0.2, 0.3, 0.4, 0.5) G-ZnO thin films were found to be (0.323, 0.024, 0.030, 0.019, 0.091, 0.026) respectively. These values are in little comparison with the values of the optical bandgap
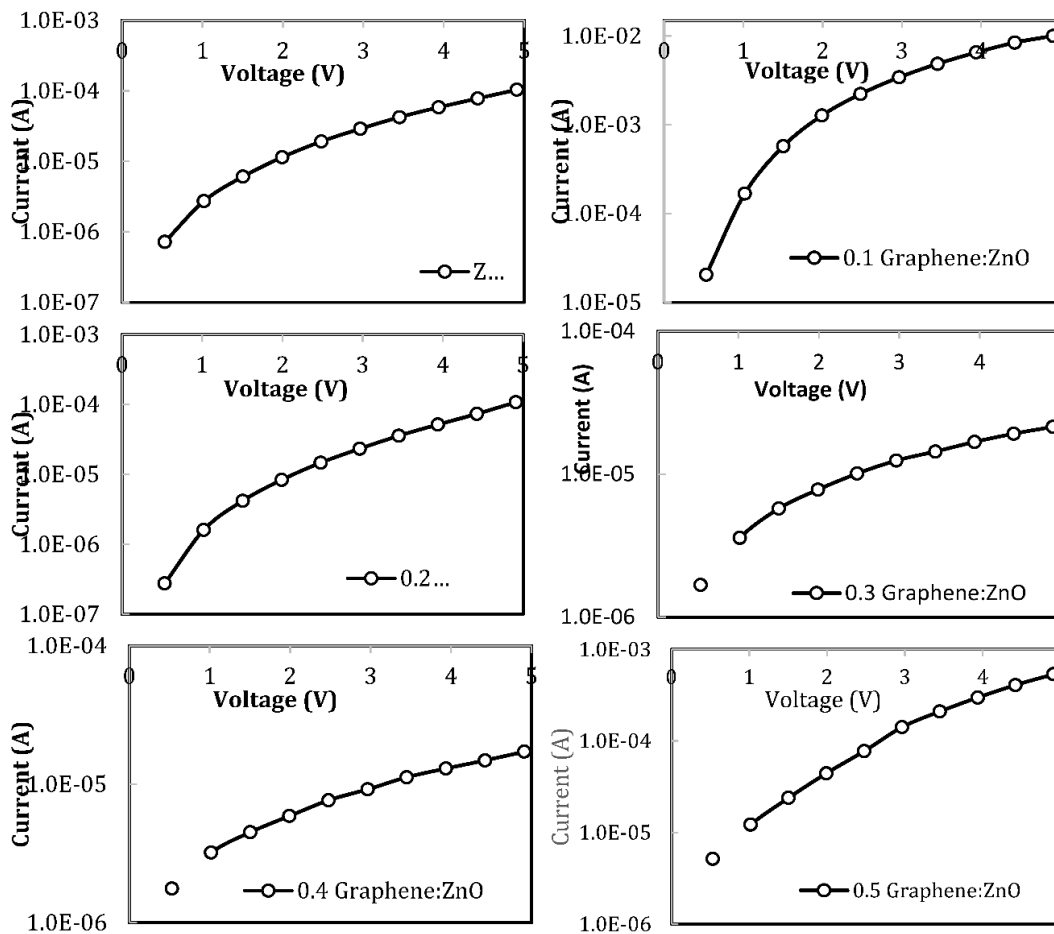

Fig. 6. Semi logarithmic plot of ln (I) and voltage (V) of G -ZnO thin films with various graphene content.

Table 2. The Ideality factor of graphene-ZnO thin films with different content.

G- ZnO concentration	Ideality factor
ZnO	2.64
0.1 G	3.9
0.2 G	1.2
0.3 G	1.9
0.4 G	1.03
0.5 G	1.12

energy of prepared thin films. This suggested that ΔEII values coincide with the level of shallow donor. This level location alteration with the graphene concentration. The (0.2, 0.3, 0.5) G-ZnO conductivity displays a linear zone and ZnO sample electrical conductivity variations with graphene concentration. The electrical conductivity of the ZnO films is lesser than that of G-ZnO film and the highest value at (0.5 G) concentration. This means that the nanostructure of graphene advances the ZnO electrical conductivity. This behavior agrees with [22].

The dark I-V characterization of the G-ZnO/Si heterojunction fabrication with various concentrations of graphene in both forward and reverse bias (-5 - 5) volt at room temperature is shown in Fig. 5. As shown in Figure, the output current increased consistently with an increase in bias voltage, demonstrating typical rectification properties. From the figure, three featured sections (I, II, and III) can see which rely on the applied voltage device in the forward bias. The first region I (V≤ 0.6 V), current obeys Ohmic law, is where the apparatus reveals a linear rise in output current.

This device attitude can refer to the tunneling current that controls the output of the device. Region 2 is where an exponential rise is observed in the output current. This technique is usually watched in broad bandgap semiconductor heterojunction diodes due to the increase in tunneling resulting from controlling recombination. When the bias voltage rises in the device in the last region, characteristics depart from the ideal thermionic emission. This difference in characteristics can denote the current conduction in the apparatus that is finite to the space charge, which is the ordinary attitude in broad bandgap materials [23,24].

For the reverse direction, the I-V heterojunction curve can recognize through two regions, the first at low voltage, in which the reverse current relies on the applied voltage. In contrast, at rising bias voltage, the width of the depletion region is enlarged, and the created current is predominant. In the second region, rise voltage is watched via a rise in the reverse bias; the diffusion current is prevalent and relies on voltage.

I-V characterization of a G-ZnO/p-Si heterojunction estimated at various content in the dark, by this outcome, we note that the current of forwarding bias is larger than the current of

reverse bias and the revers current for ZnO/Si at -5 Volt is (0.14 µA) while the current in 0.5 G-ZnO/Si at -5 volt increase to reach (6 µA).

The ideality factor is an essential parameter in heterojunction devices calculated from the equation 1:

$$(n = \frac{q}{KBT} \cdot \frac{\Delta V}{Ln\frac{(1)}{Is}})$$ (1)

where I is the forward current, Is is the saturation current, T the room temperature, K is the Boltzmann's constant, q is the electron charge and V the applied voltage[25]. Fig. 6) displays the semi-logarithmic plot of current versus the bias voltage. The interrupt of the straight-line region of the forward bias ln (I) -V characteristics with y-axis well give the reverse saturation current (I_s), and the slope produces the detector ideality factor. Table 2 represent the relation between ideality factor (n) and graphene concentration. The n value reaches the value of 1 as G- concentration increases. For n is more significant than (1), this indicates that the heterojunction exhibits a non-ideal behavior due to the oxide layer and the presence of surface states [26].

Fig. 7) displays the I-V curves family gained in the range for light intensity (25, 50, 75, and 100) mW/cm² for G- ZnO/Si heterojunction at different concentrations. The photocurrent will grow gradually with rising light intensity at negative bias voltage. The reverse bias voltage guides the rise in the internal electric field that refers to a growth in the segregated electron-hole pairs probability. The photocurrent rises with rising incident power intensity due to the increased number of created photo carriers in the depletion region.

This figure displays the rise in the photocurrent with rising applied reverse biasing and increased with an increase in the content of graphene attributed to the growing width of the depletion region where extra light will be absorbed inside this region. There is no photocurrent saturation with increasing intensity of light (good linearity properties). The higher current was at graphene concentration (0.5) at a power intensity of 100 mW because the presence of G leads to an increase the conductivity, as shown in the electrical properties.

The combination of graphene with ZnO is useful for applications of the light photodiode; it is indisputable that the transfer of carrier among

graphene and the semiconductor will reduction the diode barrier height that finites the performance enhancement of the graphene–semiconductor photodiode. [27]

The device capacitance was estimated at a frequency of 1 MHz as a function of applied voltage at room temperature. Fig. 8) performed C-V measurements of the junction capacitance as a bias voltage function for heterojunction synthesized at different graphene concentrations. The capacitance density reductions with growing reverse voltage, which demonstrates the extension of the depletion region with increasing reverse

voltage, arrive at the drop of the capacitance at the sides of the junction. Furthermore, it detected that the growth in capacitance, when growing graphene concentration, is a result of decreasing the structural defects and rise in the carrier's concentration, that in turn leads to a reduction in the V_{bi} value and, therefore, low width of the depletion region which in turn leads to increase capacitance value. Junction capacitance increasing can be ascribed to the uniformity of the particle that, in turn, decreases the structural defects like clustering and holes.

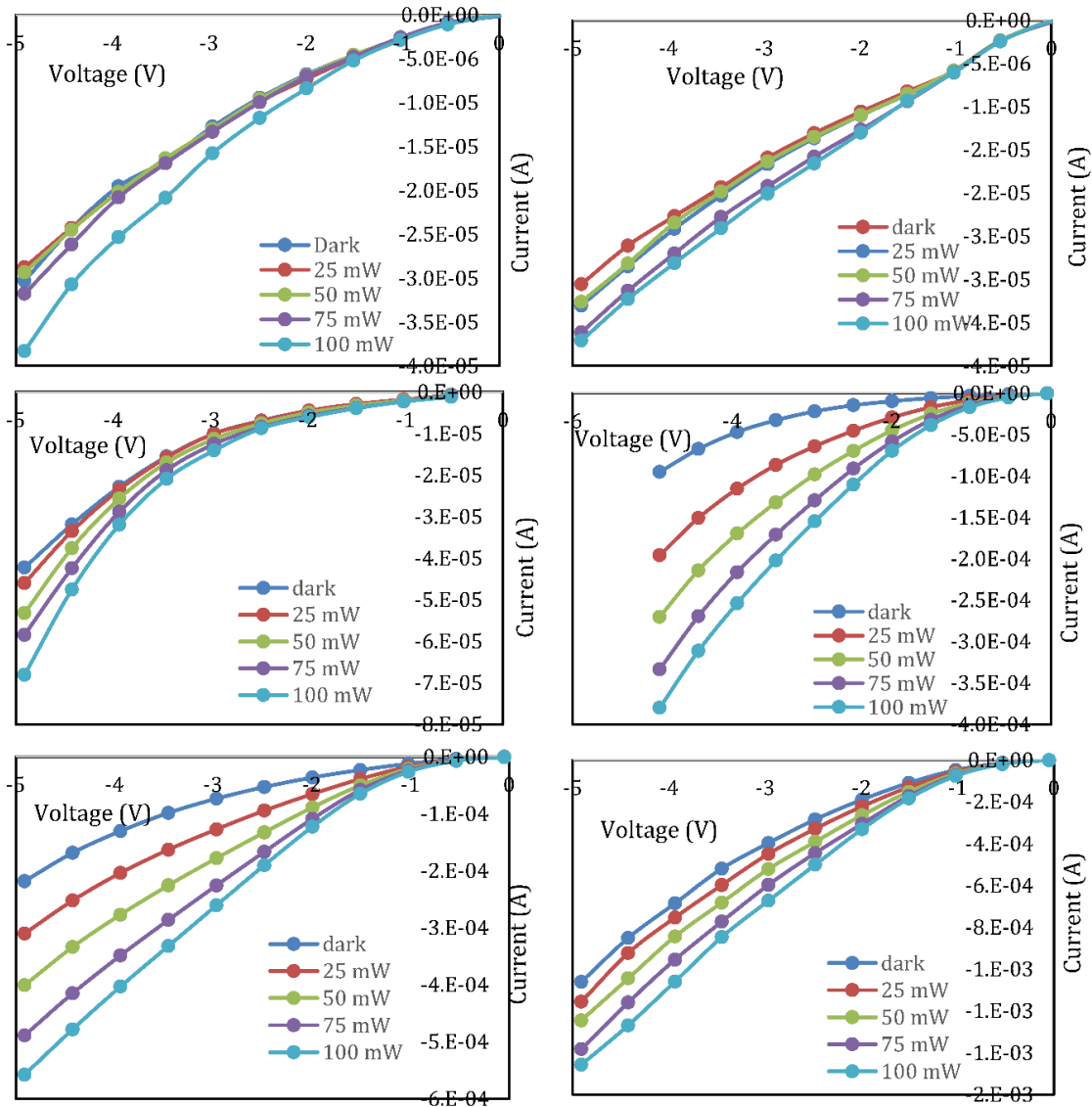The relation among squared capacitance

Fig. 7. Illuminated I-V characteristics of G -ZnO thin films with various graphene content.

reciprocal (C^{-2}) and the reverse bias at room temperature and dark for prepared heterojunction are shown in Fig. 8). The linear ship of $1/C^2$ against bias voltage indicates that the produced junction among Gr-ZnO thin film and the substrate of Si is abrupt. The built-in potential (V_{bi}) can be concluded via extrapolating the linear curve part to $1/C^2$ to zero point and recorded in the Table
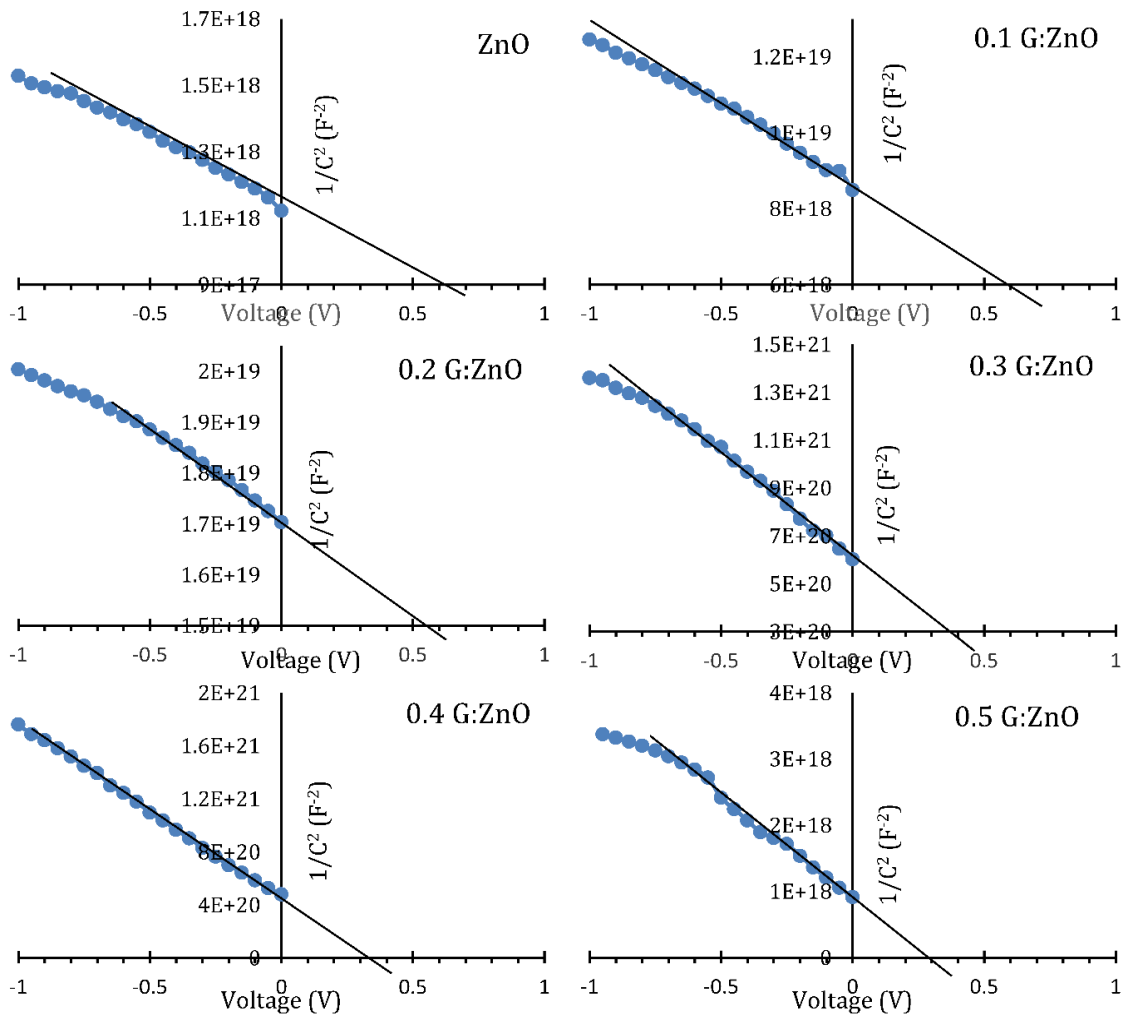

Fig. 8. $1/C^2$ versus bias voltage of the Gr-ZnO/Si prepared at different graphene concentrations.

Table 3. Built-in potential of graphene -ZnO/Si heterojunctions at different content.

G- ZnO concentration	V_{bi} (Volt)
ZnO	0.65
0.1 G	0.6
0.2 G	0.55
0.3 G	0.4
0.4 G	0.35
0.5 G	0.3

3. The achieved outcomes exhibited that the built-in potential depends on the elaboration concentration of Gr. The V_{bi} quantity for the whole of heterojunction decrease with growing the Gr. The V_{bi} value range from 0.65 V for ZnO/Si to 0.3 V for ZnO/Si with 0.5 graphene.

The spectral responsivity of the photodetector (represents the ratio among the output generated current to the incident power) is a significant parameter to estimate any photodetector performance. The spectral responsivity of the structure of Gr-ZnO/Si is examined in the range of wavelength about (200-1100) nm with a 0.5 V

bias.

Fig. 9. shows the plots of the spectral responsivity for Gr-ZnO/p-Si photodetectors produced at various graphene concentrations. These figures have two featured peaks: the first peak at 380, 400 nm (UV region), and the second peak observed at 850 nm (NIR region) with responsivity. The first peak is associated with the G-ZnO NPs absorption edge in the two suitcases, whereas the second peak results from the Si substrate absorption edge. The detection of short wavelengths occurs in the region in the ZnO layer vicinity, while the detection of long wavelengths is
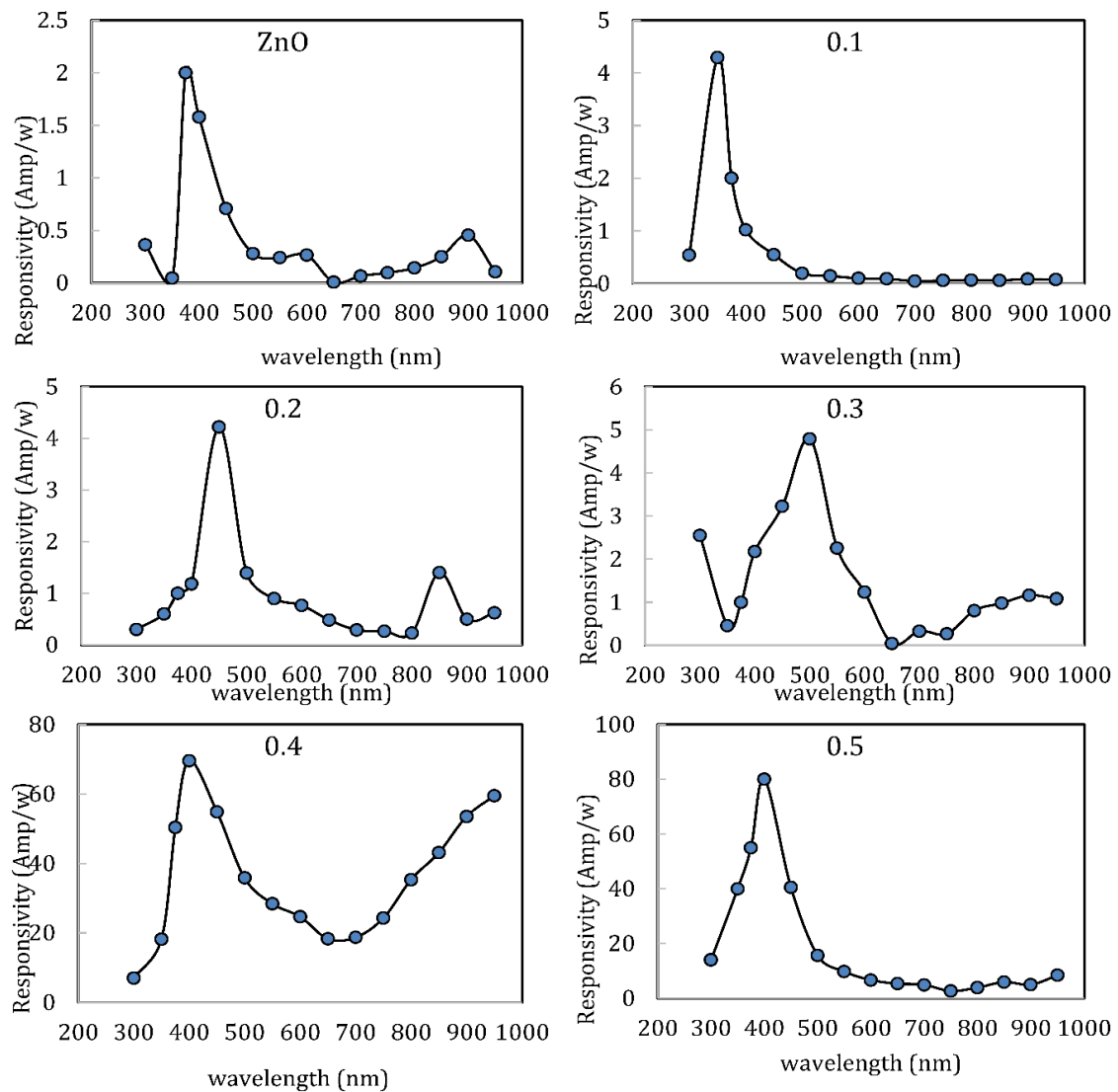

Fig. 9. Responsivity as a function of the Gr-ZnO/Si incident wavelength prepared at different graphene concentrations.

approved out at the silicon diffusion region.

Growing the graphene concentration caused the responsivity improvement since at 380, 400 nm, the responsivity was enlarged from 2 to 80 A/W. A slight shift in the spectral responsivity curve toward a long wavelength was detected after growing graphene concentration due to energy gap variation. The maximum spectral responsivity of the photodetector was noticed for G-ZnO synthesized at 0.5 Gr; this is attributed to the reality that G-ZnO synthesized at 0.5 concentration possesses greater mobility that, in turn, increases the diffusion length.

The enhancement of responsivity for photodetector may be ascribed to many reasons: Growing the diffusion length and depletion width regions, rising the light absorption, reducing the dark current, reducing the surface states, the efficiency of the carrier collection increase, and growing the area of the photodetector's absorption surface (sensitive area).

CONCLUSION

In this work, Graphene-ZnO nanohybrid thin films were effectively prepared using the spray pyrolysis technique at a substrate temperature of 350 °C. Graphene-ZnO thin films possess a well-structured crystalline hexagonal wurtzite structure with a preferred orientation over the (002) orientation. The XRD analysis has also indicated that the addition of graphene strongly affects the microstructural feature of zinc oxide films. The presence of graphene in the microstructure of the ZnO films significantly affects the grain morphology and crystalline structure of the prepared films, where the graphene nanoplate act as grain growth inhibitors. The graphene concentration in thin films affected R-T, I-V, and C-V characterization. Results confirmed that the graphene acts as an efficient modifier for the responsivity of the ZnO/Si heterojunction detector.

CONFLICT OF INTEREST

The authors declare that there is no conflict of interests regarding the publication of this manuscript.

REFERENCES

1. Silva LA, Luzardo JMM, Oliveira SM, Curti RV, Silva AM, Valaski R, et al. Graphene as interface modifier in ITO and ITO-Cr electrodes. Current Applied Physics. 2020;20(7):846-852.

2. Liang F-X, Zhang D-Y, Wang J-Z, Kong W-Y, Zhang Z-X, Wang Y, et al. Highly sensitive UVA and violet photodetector based on single-layer graphene-TiO_2 heterojunction. Opt Express. 2016;24(23):25922.

3. Hassan AI, Yahya AM. Structural and optical properties of NiO-ZnO nanocomposite thin film prepared by spray pyrolysis. AIP Conference Proceedings: AIP Publishing; 2020. p. 020208.

4. Yan X, Li J. Effect of film thickness of ZnO as the electron transport layer on the performance of organic photodetectors. Opt Mater. 2022;128:112438.

5. Chatzigiannakis G, Jaros A, Leturcq R, Jungclaus J, Voss T, Gardelis S, et al. Broadband wavelength-selective isotype heterojunction n^+-ZnO/n-Si photodetector with variable polarity. J Alloys Compd. 2022;903:163836.

6. Saimon JA, Madhat SN, Khashan KS, Hassan AI. Characterization of CdZnO/Si heterojunction photodiode prepared by pulsed laser deposition. Int J Mod Phys B. 2018;32(31):1850341.

7. Yi G-C, Wang C, Park WI. ZnO nanorods: synthesis, characterization and applications. Semicond Sci Technol. 2005;20(4):S22-S34.

8. Fan Z, Wang D, Chang P-C, Tseng W-Y, Lu JG. ZnO nanowire field-effect transistor and oxygen sensing property. Appl Phys Lett. 2004;85(24):5923-5925.

9. Paul R, Gayen RN, Biswas S, Bhat SV, Bhunia R. Enhanced UV detection by transparent graphene oxide/ZnO composite thin films. RSC Advances. 2016;6(66):61661-61672.

10. Zhang Y, Tan Y-W, Stormer HL, Kim P. Experimental observation of the quantum Hall effect and Berry's phase in graphene. Nature. 2005;438(7065):201-204.

11. Morozov SV, Novoselov KS, Katsnelson MI, Schedin F, Elias DC, Jaszczak JA, et al. Giant Intrinsic Carrier Mobilities in Graphene and Its Bilayer. Phys Rev Lett. 2008;100(1).

12. Dutta M, Sarkar S, Ghosh T, Basak D. ZnO/Graphene Quantum Dot Solid-State Solar Cell. The Journal of Physical Chemistry C. 2012;116(38):20127-20131.

13. Kavitha T, Gopalan AI, Lee K-P, Park S-Y. Glucose sensing, photocatalytic and antibacterial properties of graphene–ZnO nanoparticle hybrids. Carbon. 2012;50(8):2994-3000.

14. Li B, Cao H. ZnO@graphene composite with enhanced performance for the removal of dye from water. J Mater Chem. 2011;21(10):3346-3349.

15. Zhou X, Shi T, Zhou H. Hydrothermal preparation of ZnO-reduced graphene oxide hybrid with high performance in photocatalytic degradation. Appl Surf Sci. 2012;258(17):6204-6211.

16. Li B, Liu T, Wang Y, Wang Z. ZnO/graphene-oxide nanocomposite with remarkably enhanced visible-light-driven photocatalytic performance. Journal of Colloid and Interface Science. 2012;377(1):114-121.

17. Gong A, Feng Y, Liu C, Chen J, Wang Z, Shen T. A promising ZnO/Graphene van der Waals heterojunction as solar cell devices: A first-principles study. Energy Reports. 2022;8:904-910.

18. Fully Suspended Reduced Graphene Oxide Photodetector with Annealing Temperature-Dependent Broad Spectral Binary Photoresponses. American Chemical Society (ACS).

19. Aoun Y, Benhaoua B, Benramache S, Gasmi B. Effect of annealing temperature on structural, optical and electrical properties of zinc oxide (ZnO) thin films deposited by spray pyrolysis technique. Optik. 2015;126(24):5407-5411.

20. Liu X, Pan L, Zhao Q, Lv T, Zhu G, Chen T, et al. UV-assisted photocatalytic synthesis of ZnO–reduced graphene oxide

composites with enhanced photocatalytic activity in reduction of Cr(VI). Chem Eng J. 2012;183:238-243.

21. Qazi SJS, Rennie AR, Cockcroft JK, Vickers M. Use of wide-angle X-ray diffraction to measure shape and size of dispersed colloidal particles. Journal of Colloid and Interface Science. 2009;338(1):105-110.

22. Benhaliliba M, Benouis CE, Aida MS, Yakuphanoglu F, Sanchez Juarez A. Indium and aluminium-doped ZnO thin films deposited onto FTO substrates: nanostructure, optical, photoluminescence and electrical properties. J Sol-Gel Sci Technol. 2010;55(3):335-342.

23. Ghosh R, Basak D. Electrical and ultraviolet photoresponse properties of quasialigned ZnO nanowires/p-Si heterojunction. Appl Phys Lett. 2007;90(24).

24. Ranwa S, Kumar Kulriya P, Dixit V, Kumar M. Temperature dependent electrical transport studies of self-aligned ZnO nanorods/Si heterostructures deposited by sputtering. J Appl Phys. 2014;115(23).

25. Khashan KS, Hassan AI, Addie AJ. Characterization of CuO thin films deposition on porous silicon by spray pyrolysis. Surf Rev Lett. 2016;23(05):1650044.

26. Bedia FZ, Bedia A, Benyoucef B, Hamzaoui S. Electrical Characterization of n-ZnO/p-Si Heterojunction Prepared by Spray Pyrolysis Technique. Physics Procedia. 2014;55:61-67.

27. Liang F-X, Gao Y, Xie C, Tong X-W, Li Z-J, Luo L-B. Recent advances in the fabrication of graphene–ZnO heterojunctions for optoelectronic device applications. Journal of Materials Chemistry C. 2018;6(15):3815-3833.